SPH Simulation of Oblique Shocks in Compressible Flows

M. Silla, V. Bertola

Laboratory of Technical Physics, School of Engineering, University of Liverpool
Brownlow Hill, Liverpool L69 3GH, United Kingdom

ABSTRACT

The Lagrangian Smoothed Particle Hydrodynamics (SPH) method is used to simulate shock waves in inviscid, supersonic (compressible) flow. It is shown for the first time that the fully Lagrangian SPH particle method, without auxiliary grid, can be used to simulate shock waves in compressible flow. The wall boundary condition is treated with ghost particles combined with a suitable repulsive potential function, while corners are treated by a novel "angle sweep" technique. The method gives accurate predictions of the flow field and of the shock angle as compared with the analytical solution. The study shows that SPH is a good potential candidate to solve complex aerodynamic problems, including those involving rarefied flows, such as atmospheric re-entry.

1. INTRODUCTION

Smoothed particle hydrodynamics (SPH) is a numerical method to obtain a fluid flow field by replacing the fluid with particles which carry the material information and act as interpolation points equivalent to grid points in finite-difference schemes [1]. This means that SPH is a fully Lagrangian method, and one can avoid the grid (or mesh) generation step necessary for finite-differences, finite-volumes or finite-elements discretization techniques. The use of particles in the discretization of the flow field brings along a number of advantages. For example, different materials or fluids can be easily described by different sets of particles and the implementation of free surfaces and interfaces is often trivial for SPH, while it is generally difficult for grid-based techniques; secondly, SPH naturally bridges the gap of transition from continuum to rarefied flows (e.g. fragmentation in solids). Moreover, due to close similarity of SPH to molecular dynamics, it is possible to implement complex physics easily [2]. Quoting von Neumann, the particle method is not only an approximation of the continuum fluid equations, but also gives the rigorous equations for a particle system which

approximates the molecular system underlying, and more fundamental than the continuum equations [3].

SPH emerged later than finite-differences based methods, and was initially conceived to simulate cosmological problems [4-6]. It was extensively used to simulate a range of incompressible and non-Newtonian flows [7-9], notably many free-surface flows, including drop spreading and impact on solid surfaces [10,11]. Recently, the SPH method has been applied to simulate flow instabilities at the interface between two fluids [12-13], as well as the flow in porous media [14]. SPH has also found applications in the area of computer graphics, mainly to simulate water and multibody interactions, due to its ease of dealing complex, time-dependent boundaries and multibody interactions with flows [15].

However, perhaps due to historical reasons, SPH is not widely used for aerodynamics problems where finite-volume and finite-differences techniques are usually preferred. Recently, the SPH approach was proposed to simulate shock wave reflections in a shock tube with a wedge [16]. However, in this work particles were regularized periodically during the simulation by superimposing a grid to the problem domain, and redistributing particles evenly to reduce the discretization errors associated with the aggregation of particles. Therefore it introduces an additional step, which makes the method less straightforward and increases the computational cost.

This work implements a mesh-free SPH method for treating fluid dynamics problems relevant to aerodynamics, specifically the two-dimensional compression corner problem which looks at supersonic flow encountering sharp inward turn, resulting in the formation of an oblique shock, as shown schematically in Figure 1. This problem was investigated due to its simplicity and the fact that it lends itself to closed form analytical solution for shock angle, given that shock is not detached, and fluid is an inviscid calorically perfect gas.

The proposed SPH formulation assumes inviscid flow, and constant smoothing lengths in the particle approximation; boundaries are treated using ghost particles and a Lennard-Jones repulsion potential near walls. Various smoothing kernels are implemented along with explicit Monaghan artificial viscosity to resolve shocks.

2. SPH FORMULATION

The first step in deriving the SPH method is to develop an integral representation of the field function which is approximated by summation of neighbouring particles in the smoothing domain, multiplied by a smoothing function. The smoothing function weighs the field

variables according to their distance from the interpolation particle, so that particles closer to the interpolation particle contribute more. The integral form is written as

$$f(\boldsymbol{x}) = \int f(\boldsymbol{x}')\delta(\boldsymbol{x} - \boldsymbol{x}')d\boldsymbol{x}' \tag{1}$$

where f(**x**) is a function of the three-dimensional position vector **x** and is integrated over the volume that contains **x**, and δ(**x**-**x**') is Dirac's delta function, which means that Eq. (1) produces exactly the function f(**x**). This integral representation is then modified to account for the influence of neighbouring particles on the particle of interest. This is achieved by replacing the Dirac delta by a smoothing function, or kernel, W(**x**-**x**',h):

$$f(\boldsymbol{x}) = \int f(\boldsymbol{x}')W(\boldsymbol{x} - \boldsymbol{x}', h)d\boldsymbol{x}' \tag{2}$$

The smoothing function has to satisfy a number of conditions, extensively discussed in the literature (e.g., [17]).

Now, the infinitesimal volume $d\boldsymbol{x}'$ is replaced by ΔV_j ,corresponding to the j-th particle and then Eq. (2) can be written in terms of particle summation over the support (smoothing) domain of N particles as

$$f(\boldsymbol{x}) \cong \sum_{j=1}^{N} f(\boldsymbol{x_j})W(\boldsymbol{x} - \boldsymbol{x_j}, h)\Delta V_j \tag{3}$$

or

$$f(\boldsymbol{x}) \cong \sum_{j=1}^{N} f(\boldsymbol{x_j})W(\boldsymbol{x} - \boldsymbol{x_j}, h)\frac{m_j}{\rho_j} \tag{4}$$

Defining $W(\boldsymbol{x_i} - \boldsymbol{x_j}, h) = W_{ij}$, Eq. (4) becomes

$$f(\boldsymbol{x_i}) = \sum_{j=1}^{N} \frac{m_j}{\rho_j} f(\boldsymbol{x_j}) \cdot W_{ij} \tag{5}$$

This is the particle approximation for any function according to the SPH formulation, and similar manipulations can be used to show that divergence of any function is,

$$\nabla \cdot f(\boldsymbol{x_i}) = \sum_{j=1}^{N} \frac{m_j}{\rho_j} f(\boldsymbol{x_j}) \cdot \nabla_i W_{ij} \tag{6}$$

This result has important consequences, and in particular the spatial gradient of any function is found by simply taking the gradient of the smoothing function.

The conversion of Navier-Stokes equations to particle approximation using Eqs. (5-6) is extensively discussed in the literature, for example [17]. The resulting equations conserve

linear and angular momentum [1], and for unsteady, inviscid flow without body forces in two dimensions they can be written as:

$$\frac{D\rho_i}{Dt} = \sum_{j=1}^{N} m_j \boldsymbol{V}_{ij} \cdot \begin{pmatrix} \frac{\partial W_{ij}}{\partial x_i} \\ \frac{\partial W_{ij}}{\partial y_i} \end{pmatrix} \tag{7}$$

$$\frac{Du_i}{Dt} = -\sum_{j=1}^{N} m_j \left(\frac{p_i}{\rho_i^2} + \frac{p_j}{\rho_j^2}\right) \frac{\partial W_{ij}}{\partial x_i} \tag{8}$$

$$\frac{Dv_i}{Dt} = -\sum_{j=1}^{N} m_j \left(\frac{p_i}{\rho_i^2} + \frac{p_j}{\rho_j^2}\right) \frac{\partial W_{ij}}{\partial y_i} \tag{9}$$

$$\frac{De_i}{Dt} = \frac{1}{2}\sum_{j=1}^{N} m_j \left(\frac{p_i}{\rho_i^2} + \frac{p_j}{\rho_j^2}\right) \boldsymbol{V}_{ij} \cdot \begin{pmatrix} \frac{\partial W_{ij}}{\partial x_i} \\ \frac{\partial W_{ij}}{\partial y_i} \end{pmatrix} \tag{10}$$

In the present work, the flow field is solved for every particle with respect to primitive variables of density ρ_i, velocity components in the x and y direction (u_i, v_i) and internal energy e_i, using an explicit leapfrog time marching scheme with second-order accuracy. Pressure, internal energy and density are connected through the ideal gas equation of state,

$$p = (\gamma - 1)\rho e \tag{11}$$

where γ is the ratio of specific heats.

3. SPH IMPLEMENTATION FOR A COMPRESSION CORNER

The compression corner problem is sketched in Figure 1; a gas flow with initial Mach number $M_1 > 1$ is deflected in a sharp corner, with a deflection angle θ with respect to the incoming flow direction, and as a consequence there is an oblique shock at an angle β with respect to the same incoming flow direction. Figure 1 also displays the different boundary conditions. Firstly, boundary treatment was implemented by using ghost particles at the boundaries; these particles are generated at each time step outside of the computational domain, and inherit the flow field properties from particles they are generated from. In the generation process, all particles in the vicinity of a boundary (i.e., when the particle support domain is

partly outside of problem domain), are mirrored to the opposite side of the boundary. Ghost particles were used at the domain boundaries by mirroring particles to the outside of the problem domain (with respect to the boundary itself), while keeping all the flow field variables identical. This is purely to convey the illusion that the flow is present even beyond problem domain and not cause any unwanted accelerations, and discretization errors. Ghost particles ensure that the support domains of particles are not truncated, to avoid an artificial force pushing particles towards empty areas, as shown in Figure 1. Error analysis shows that to obtain convergence: $N_t \to \infty$, $N \to \infty$ and $h \to 0$, where N_t is the total number of particles in problem domain and h is smoothing length which defines the size of support domain [18]. This shows that if some particles are lost at boundaries, the solution accuracy is affected significantly.

Whilst ghost particles ensure an appropriate treatment of the free (upper and inlet) boundary of the computational domain, they are not sufficient at rigid wall boundaries; in this case, particles would penetrate wall despite presence of ghost particles, as these would merely appear to be a fluid (air) at the boundary. To eliminate this effect, an additional Lennard-Jones-like wall repulsion force was introduced along solid wall boundaries, which can be written as [17]:

$$\boldsymbol{f}_r = \begin{cases} D\left[\left(\frac{r_0}{r_{ij}}\right)^{12} - \left(\frac{r_0}{r_{ij}}\right)^{6}\right]\frac{\boldsymbol{x}_{ij}}{{r_{ij}}^2} & \left(\frac{r_0}{r_{ij}}\right) > 1 \\ 0 & \left(\frac{r_0}{r_{ij}}\right) \leq 1 \end{cases} \tag{12}$$

where $D = a * [max(V)^2]$, and a is a positive constant adjusted empirically (in the simulations reported below, a = 0.65); the activation distance for the force r_0 is equal to the initial particle spacing, r_{ij} is distance between the wall and the particle, and $\boldsymbol{x}_{ij}$ is the vector from the wall to the particle. This force term is added to the right hand side of momentum equations, and results in a large force gradient as particles approach imaginary wall boundary particles. Thus, ghost particles and the wall force must be used concurrently in order to get physically significant results.

This kind of treatment at solid boundary differs from finite-difference-like schemes, where it is very convenient to force velocities to zero when discretization point lies on the boundary but more difficult in SPH where the particle approaching the wall must be decelerated by some force, in this case given by Eq. (12).

The boundary treatment at corners is more complex. The mirroring of particles normal to two walls simultaneously (in 2D) results in empty regions outside of problem domain, as one can see in Figure 1. To address this problem, a generalization of the standard particle mirroring method was introduced, which is schematically illustrated in Figure 3: (i) for small deflection angles of the boundary ($\theta \leq 90°$, Figure 3a), the mirroring axis was defined as the bisector of the deflection angle; for large deflection angles ($\theta > 90°$, Figure 3b), the external area lacking ghost particles was divided into a finite number of angular sectors and the same number of mirroring axes were defined perpendicular to the bisector of each angular region; particles were then mirrored with respect to each mirroring axis. The optimal amplitude of the angular sectors is the one that maximises the coverage of ghost particles in the outer region of the corner, however a sensitivity analysis shows the sector amplitude does not affect simulations significantly. This procedure can be easily extended to a three-dimensional case, and to our knowledge was never used before; we remark this peculiar boundary treatment is not necessary in standard sub-sonic SPH simulations, therefore it represents one of the innovative contributions of our work.

In order to simulate flows, there must be a periodic introduction of particles at the domain inlet; this was done by setting a time step such that particles can be introduced after *cn* time steps so that mass flow rate is constant and matches the continuum inlet value. Both the outlet and the inlet boundaries are handled similarly to other boundaries for which ghost particles are generated.

Artificial viscosity is added to ensure that shock waves are captured; this is similar to some shock capturing finite-difference schemes which require an artificial viscosity to smooth oscillations near shocks, which are generated because in the discretised implementation, interpolation nodes receive information from both sides of the shock, which is not physically admissible. The following artificial viscosity term was added to the momentum and energy equations [17]:

$$\Pi_{ij} = \begin{cases} \dfrac{-\alpha_\Pi \bar{c}_{ij} \phi_{ij} + \beta \phi_{ij}^2}{\bar{\rho}_{ij}} & \boldsymbol{v}_{ij} \cdot \boldsymbol{x}_{ij} < 0 \\ 0 & \boldsymbol{v}_{ij} \cdot \boldsymbol{x}_{ij} \geq 0 \end{cases} \tag{13}$$

where

$$\phi_{ij} = \frac{h_{ij} \boldsymbol{v}_{ij} \cdot \boldsymbol{x}_{ij}}{\left|\boldsymbol{x}_{ij}\right|^2 + \varphi^2} \tag{14}$$

and $\varphi = 0.1h_{ij}$ to prevent numerical divergence when two particles come close to each other.

Two different kernels were tested, more precisely a quartic kernel and a standard cubic spline. The quartic kernel proved to be computationally more effective, and its performance was similar to cubic spline.

The overall number of particles was not specified before the start of simulations; instead, the selected input parameter was the particle density f, defined as:

$$f = \frac{\tilde{L}}{n} \tag{15}$$

where n is the number of particles to be placed along the domain inlet and $\tilde{L}$ is the characteristic length, which in this case was set equal to the inlet height of the computational domain.

The time step for the simulations was given by:

$$dt = c\left(\frac{h}{a_0}\right) \tag{16}$$

where a_0 is the stagnation speed of sound and c is the Courant number. Stable simulation runs were achieved when roughly c ≤ 0.2.

Figure 4 displays the flow chart of the SPH solver. First, particles are initialized all over the domain; the second step is to treat boundaries by creating ghost particles, which is followed by particle search to determine the position of each particle within the support domain of every other particle, to enable subsequent calculations. Next, kernel functions and kernel derivatives are computed for every interacting pair of particles. This is followed by solving the algebraic Eqs. (7-10), after which time is advanced according to the leapfrog scheme. Finally, particles crossing the problem domain are eliminated and new particles are introduced at the inlet.

4. RESULTS

To test the suitability of SPH for compressible aerodynamics, a simple two-dimensional compression corner was selected as the benchmark case, since the exact analytical solution for the shock angle is available:

$$tan\theta = 2cot\beta\left[\frac{M_1^2 \sin^2\beta - 1}{M_1^2(\gamma + cos2\beta) + 2}\right] \tag{17}$$

where θ is the wedge angle and β the shock wave angle (see e.g. [19] and Figure 1).

A total of six cases with varying wedge angle at $M_1 = 3.8$ and $\gamma = 1.4$ were simulated, as shown in Table 1. These test cases were simulated with parameters $f = 1/60$ and $N = 22.5$.

This yields approximately $N_t = 10^4$ particles for the simulation at steady state. Figure 5 illustrates one example of simulation, where the particle nature of this method and the unsteady shock formation can be observed.

Results for an entire set of wedge angles are displayed in Figure 6, where red crosses denote SPH solutions and error bars associated with these represent the standard error in the angle measurements. Figure 7 shows one metric of convergence to steady state, namely the net mass flow into the problem domain.

It can be seen from Figure 6 and Table 1 that SPH produces very accurate results for a wide range of wedge angles. The standard error reported in Table 1 is an estimate of the error on the shock angle measured from the simulations output, which was done by picking three values along the steady shock region. The average relative error with respect to theoretical shock angle is very small and generally of the order of one to two percent.

Other than the measurement error, the accuracy of simulations relative to the theoretical values depends on a number of reasons. Firstly, there was a slight discrepancy between the assigned and the observed values of the free-stream flow field variables, which was probably caused by particles packing; the inlet particles were not distributed according to the highest-density face centred lattice configuration but according to a square lattice. Secondly, in the vicinity of the shock, the particle support domains may cross the shock itself, thus violating the information transfer principle [20]. Thus, in order to make simulations stable, an artificial viscosity was introduced, which is a source of errors itself. An example of the effect of the particle density f on the shock angle accuracy, for the case of a wedge angle of $25°$ is displayed in Figure 8.

The convergence behaviour of this method shows three main stages. At the beginning, particles are introduced into the domain but none of them leave the domain. Then, as particles start to exit from the domain and the shock wave begins to develop, one can observe a rapid convergence of the net mass inflow which eventually approaches the steady-state plateau at large computation times.

Even though the net mass inflow into problem domain is not exactly zero, for all practical purposes shock waves are resolved with sufficient accuracy, and become steady at large times for all observed simulations.

Figure 9 shows examples of contour maps for the Mach number, density and stagnation enthalpy; it can be seen that Mach numbers (Figure 9a) are uniform upstream of the shock and essentially uniform downstream of the shock. The shock discontinuity is captured with a satisfactory resolution, i.e., similar to grid based shock capturing schemes, bearing in mind

that SPH and grid based methods are both far off in resolving shock as a discontinuity of the order of few molecular mean free paths ($\approx 10^{-7}$ m). A closer look at the region near the wall reveals the existence of some fluctuations, which can be observed both in the Mach number and in the density (Figure 9b) plots, and are thought to be caused by the tendency of particles to aggregate in non-uniform manner inducing discretization errors, which might result from the ghost particles boundary treatment. In particular, the boundary force was found to slightly affect energy conservation near solid walls by doing work on particles as they approach the wall, and fall within the Lennard-Jones activation distance; in fact, if the force is applied when the particle is moving in the force direction, it means energy is into the system, however such input energy is not cancelled by the work extracted from the domain as particles are decelerated. One evidence in support of this scenario is the increased stagnation enthalpy at the walls, which is visible in Figure 9c. This suggests these fluctuations may be reduced or suppressed for example by fine tuning of the artificial viscosity.

5. CONCLUSIONS

The proposed SPH implementation shows for the first time that SPH can be used to reliably simulate supersonic aerodynamics. Validation was carried out using the compression corner benchmark and demonstrated that SPH can produce accurate simulations of shock waves over a range of wedge angles in supersonic flow.

Because of the intrinsic mesh-free nature of SPH, the proposed algorithm could be readily extended to simulate aeroelastic problems where there is coupling between solid wall and fluid; in that case, the solid object is represented by another set of particles.

The proposed implementation could be further refined introducing: an upward differentiation scheme for consistency and better boundary treatments; implicit time stepping; viscid three-dimensional flow simulation capability.

REFERENCES

1. Monaghan, J. J. (2005). Smoothed particle hydrodynamics. Reports on Progress in Physics, 1703-1759.
2. Litvinov, S., Ellero, M., Hu, X., and Adams, N.A. (2008) Smoothed dissipative particle dynamics model for polymer molecules in suspension, Physical Review E 77, 066703 .
3. Von Neumann, J. (1944) Proposal and analysis of a new numerical method for the treatment of hydrodynamical shock problems, Institute of Advanced Study, Princeton, N. J. March 1944.

4. Lucy, L.B. (1977) 'A numerical approach to the testing of the fission hypothesis', The astronomical journal, vol. 82, pp. 1013-1024.
5. Gingold, R.A. & Monaghan, J.J. (1977) 'Smoothed particle hydrodynamics-theory and application to non-spherical stars', Monthly notices of the royal astronomical society, vol. 181, pp. 375-389.
6. Beck, A. M., Murante, G., Arth, A., Remus, R.-S., Teklu, A. F., Donnert, J. M., Borgani, S. (2015). An improved SPH scheme for cosmological simulations. Monthly Notices of the Royal Astronomical Society, 1-22.
7. Liu, M. & Liu, G. (2010) 'Smoothed particle hydrodynamics (SPH): an overview and recent developments', Archives of computational methods in engineering, vol. 17, no. 1, pp. 25-76.
8. Ellero, M., Kröger, M. & Hess, S. (2002) 'Viscoelastic flows studied by smoothed particle dynamics', Journal of Non-Newtonian Fluid Mechanics, vol. 105, no. 1, pp. 35-51.
9. X.-J. Fan, R.I. Tanner, R. Zheng (2010), Smoothed particle hydrodynamics simulation of non-Newtonian moulding flow, J. Non-Newtonian Fluid Mech. 165 pp. 219–226.
10. E.Y.M. Lo, S. Shao (2002) Simulation of near-shore solitary wave mechanics by an incompressible SPH method, Appl. Ocean Res. 24 pp. 275.
11. L. Wieth, S. Braun, R. Koch, H.-J. Bauer (2014) Modeling of liquid-wall interaction using the meshless Smoothed Particle Hydrodynamics (SPH) method, ILASS – Europe 2014, 26th Annual Conference on Liquid Atomization and Spray Systems, Sep. 2014, Bremen, Germany.
12. Rahmat, A., Tofighi, N., Shadloo, M. & Yildiz, M. (2014) 'Numerical simulation of wall bounded and electrically excited Rayleigh–Taylor instability using incompressible smoothed particle hydrodynamics', Colloids and Surfaces A: Physicochemical and Engineering Aspects.
13. Shadloo, M.S. & Yildiz, M. (2011) 'Numerical modeling of Kelvin–Helmholtz instability using smoothed particle hydrodynamics', International Journal for Numerical Methods in Engineering, vol. 87, no. 10, pp. 988-1006.
14. Holmes, D.W., Williams, J.R. & Tilke, P. (2011) 'Smooth particle hydrodynamics simulations of low Reynolds number flows through porous media', International Journal for Numerical and Analytical Methods in Geomechanics, vol. 35, no. 4, pp. 419-437.

15. Becker, M., & Teschner, M. (2007). Weakly compressible SPH for free surface flows. Eurographics/ ACM SIGGRAPH Symposium on Computer Animation (pp. 1-8). San Diego: Association for Computing Machinery (ACM).
16. Omang M. ,· Børve S., Trulsen· J. (2006) Numerical simulations of shock wave reflection phenomena in non-stationary flows using regularized smoothed particle hydrodynamics (RSPH), Shock Waves 16 pp. 167–177.
17. Liu, G. R., & Liu, M. B. (2003). Smoothed Particle Hydrodynamics : A Meshfree Particle Method. -: World Scientific Publishing Co.
18. Zhu, Q., Hernquist, L., & Li, Y. (2015). Numerical convergence in smoothed particle hydrodynamics. The Astrophysical Journal, 1-13.
19. Anderson, J. D. (2004). Modern Compressible Flow With Historical Perspective (3rd, International Edition ed.). Singapore: McGraw-Hill.
20. Anderson, J. D. (1995). Computational Fluid Dynamics The Basics with Applications. Singapore: McGraw-Hill.

Table 1. Compression corner test cases.

Case	θ (°)	β (°)	$\beta_{theoretical}$ (°)	Standard error (°)	ε (%)
1	15	28,57	27,83	0,09	2,65
2	20	34,22	33,23	0,28	2,98
3	25	39,84	39,25	0,04	1,49
4	30	46,60	46,10	0,14	1,08
5	35	56,10	54,67	0,50	2,62
6	38	64,00	64,19	3,01	0,296

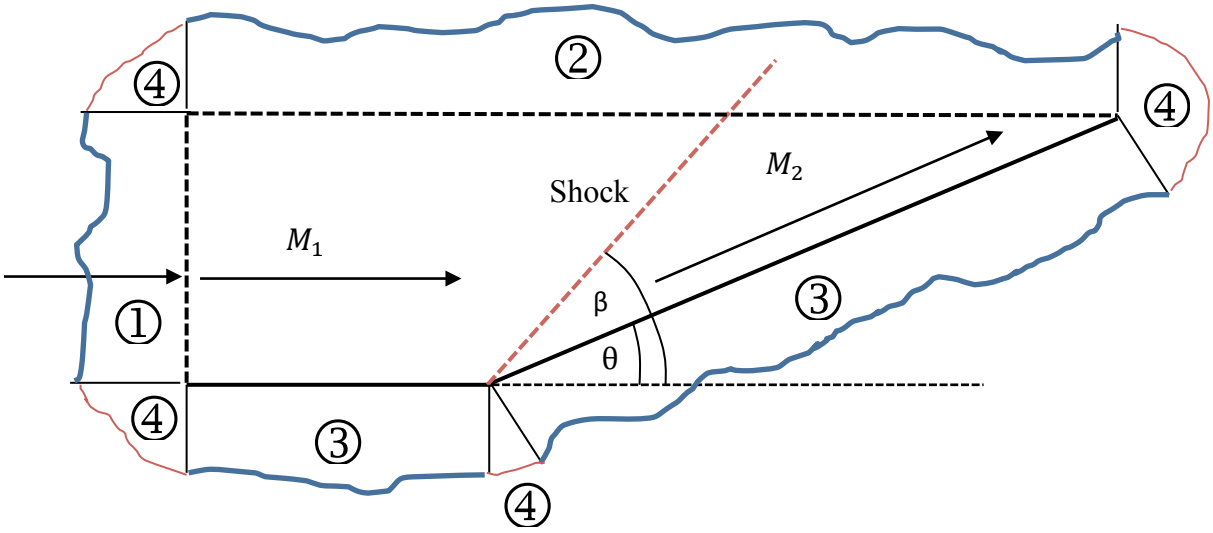

Figure 1. Schematic of the compression corner with boundary treatment and ghost particles distribution: (1) inlet boundary with supersonic flow; (2) free boundary, ghost particles, identical flow field variables; (3) wall boundary, inviscid (**V**·**n**=0), enforced by force; (4) deficient corner regions, corner treatment (see main text for details).

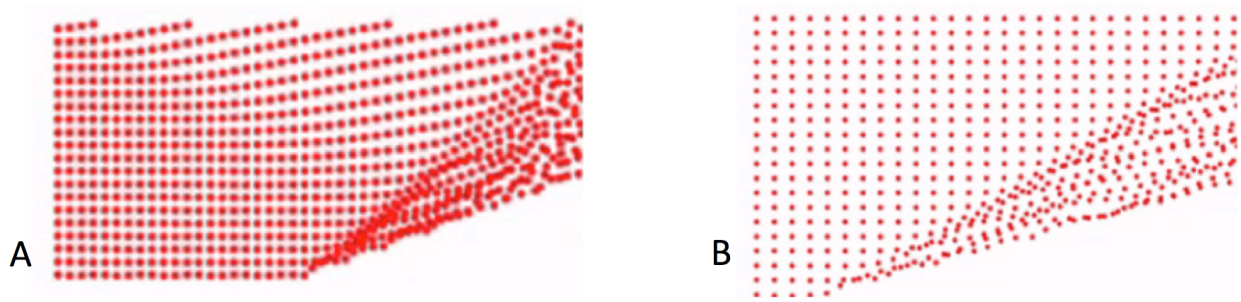

Figure 2. Solid wall boundary treatment; (a) absence of ghost particles generates an expansion wave that propagates towards the upper boundary (note particle trajectories are deflected upwards); (b) when ghost particles, this effect disappears.

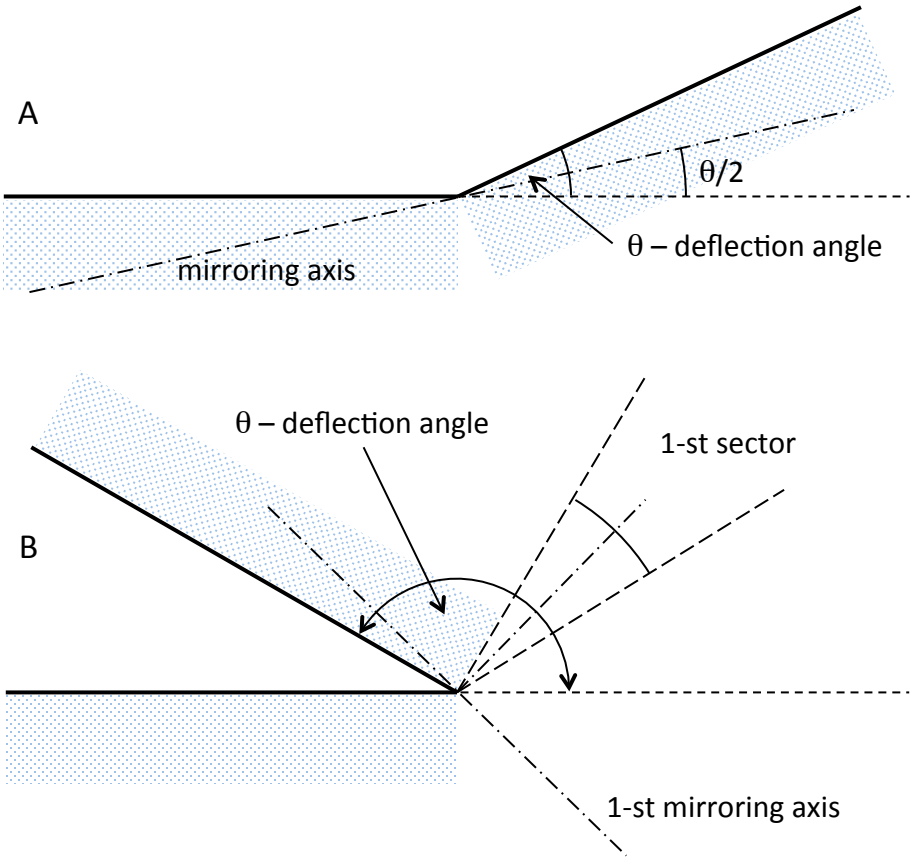

Figure 3. Schematic of corner treatment: (a) small deflection angles; (b) large deflection angles. The shaded areas indicate the regions where paerticles are mirrored using the standard mirroring procedure using the wall as mirroring axis.

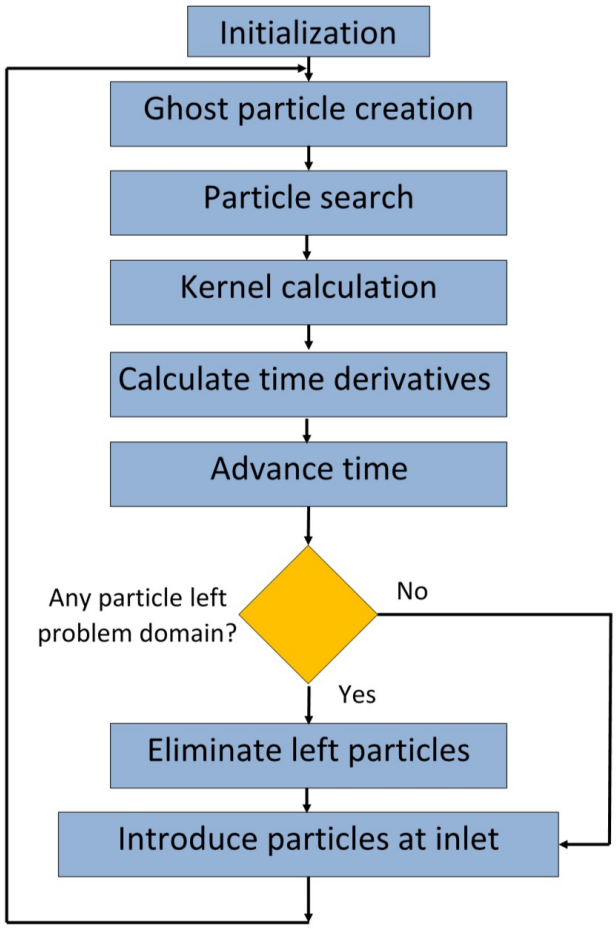

Figure 4. Algorithm flow-chart.

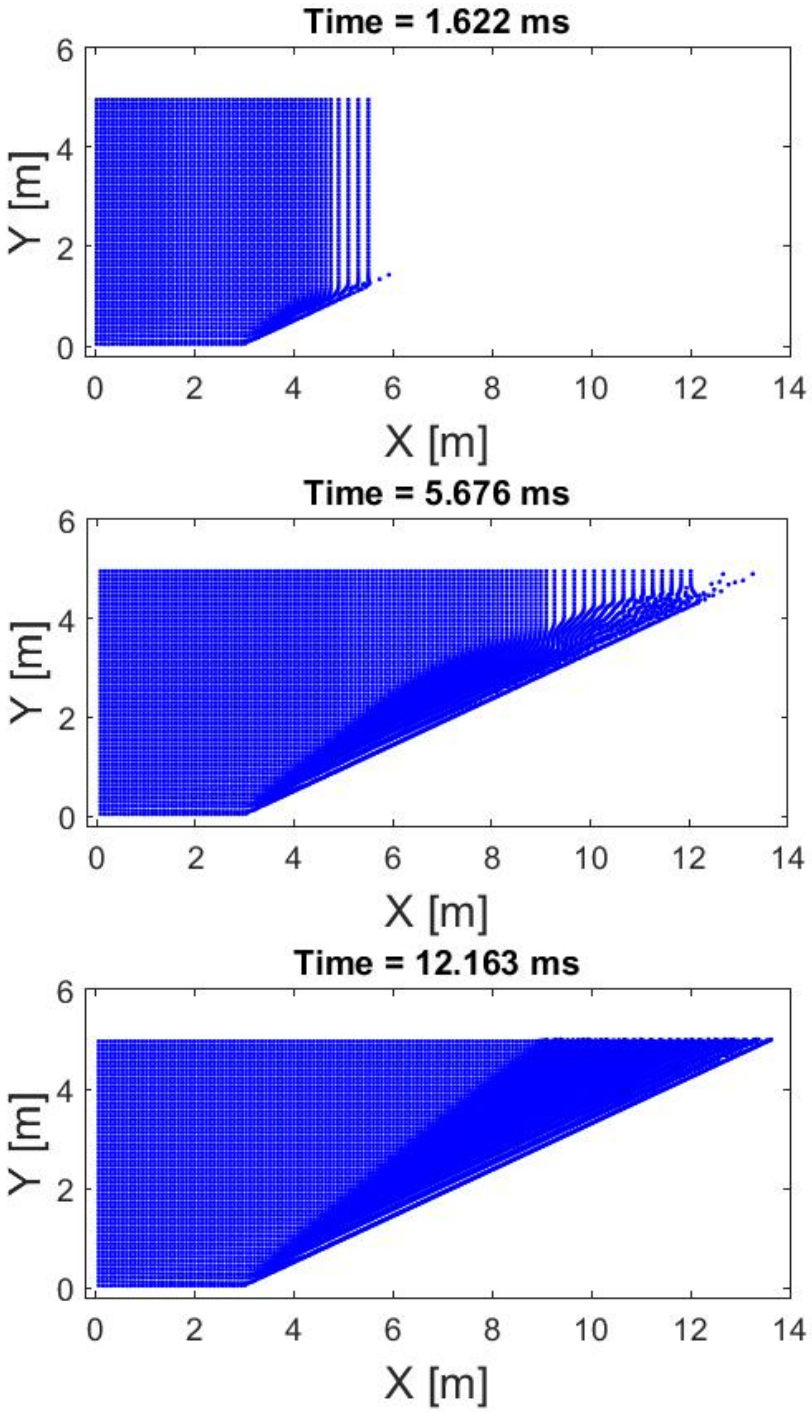

Figure 5. Example of simulation results during the transient.

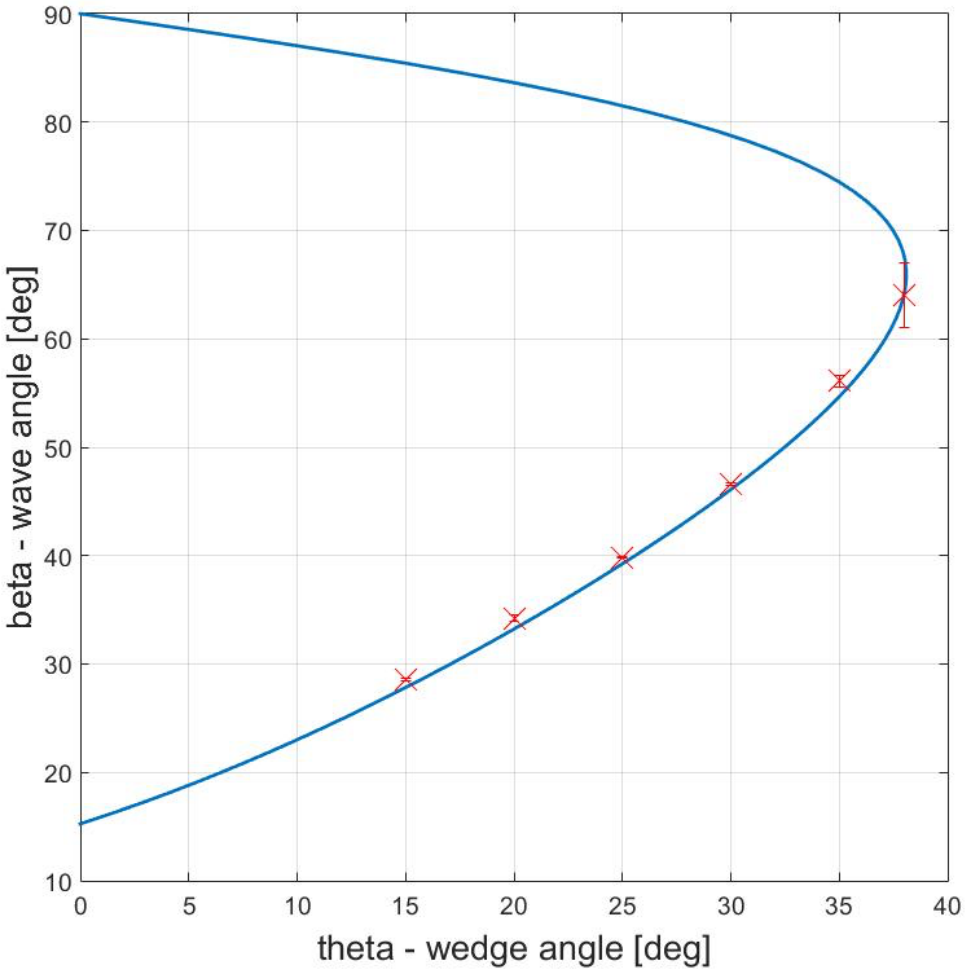

Figure 6. Shock angles for different wedge angles of the compression corner; the blue solid line represents the exact analytical solution and red crosses with error bars the SPH results.

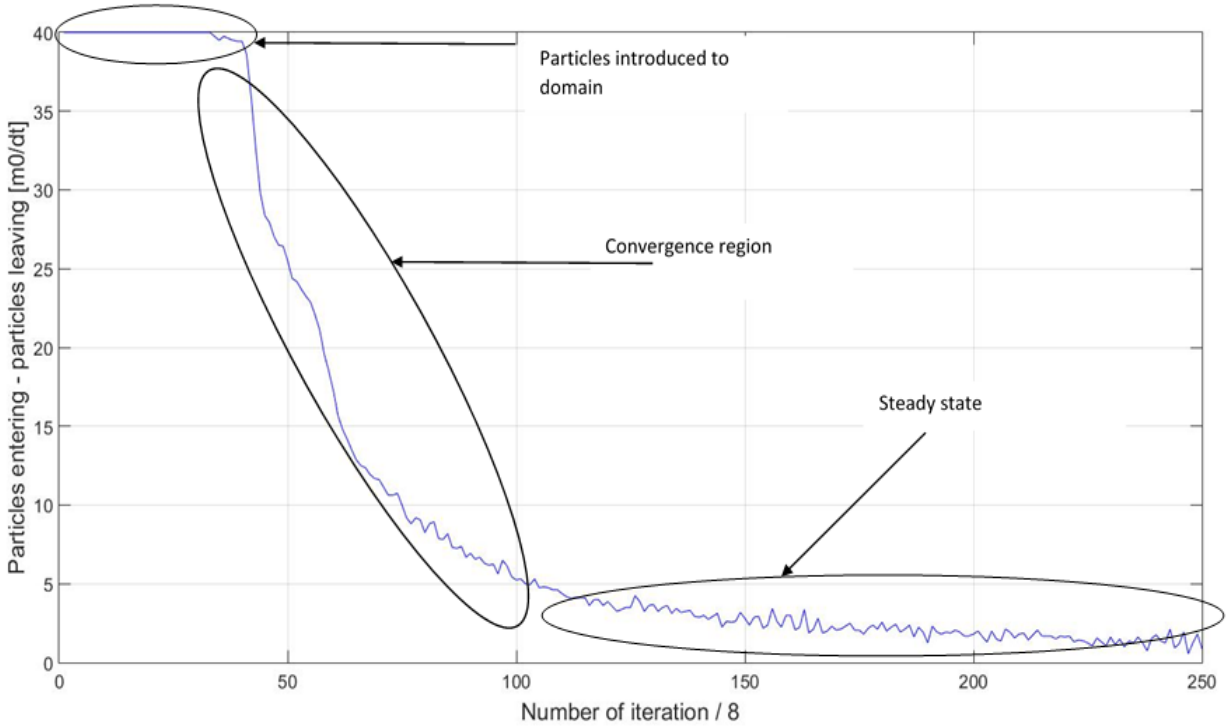

Figure 7. Algorithm convergence measured by the net mass inflow into the computational domain.

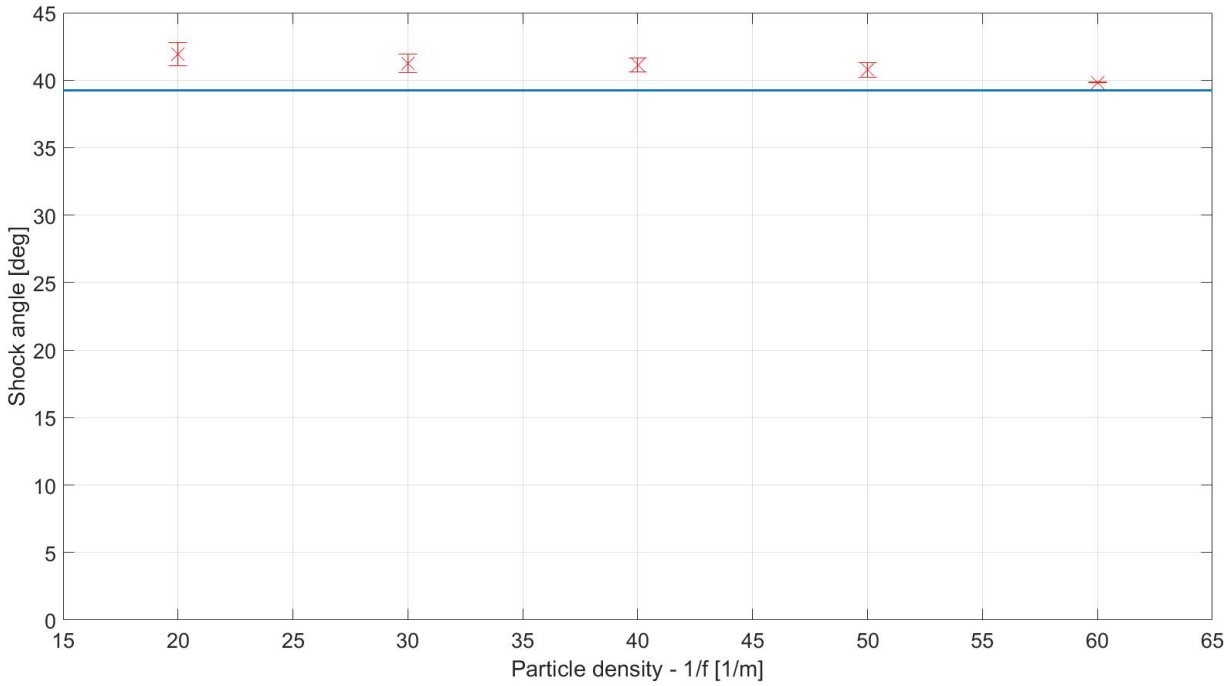

Figure 8. Convergence of the computed shock angle with respect to particle density for test case No. 3 ($\theta = 25°$); the solid line represents the theoretical value.

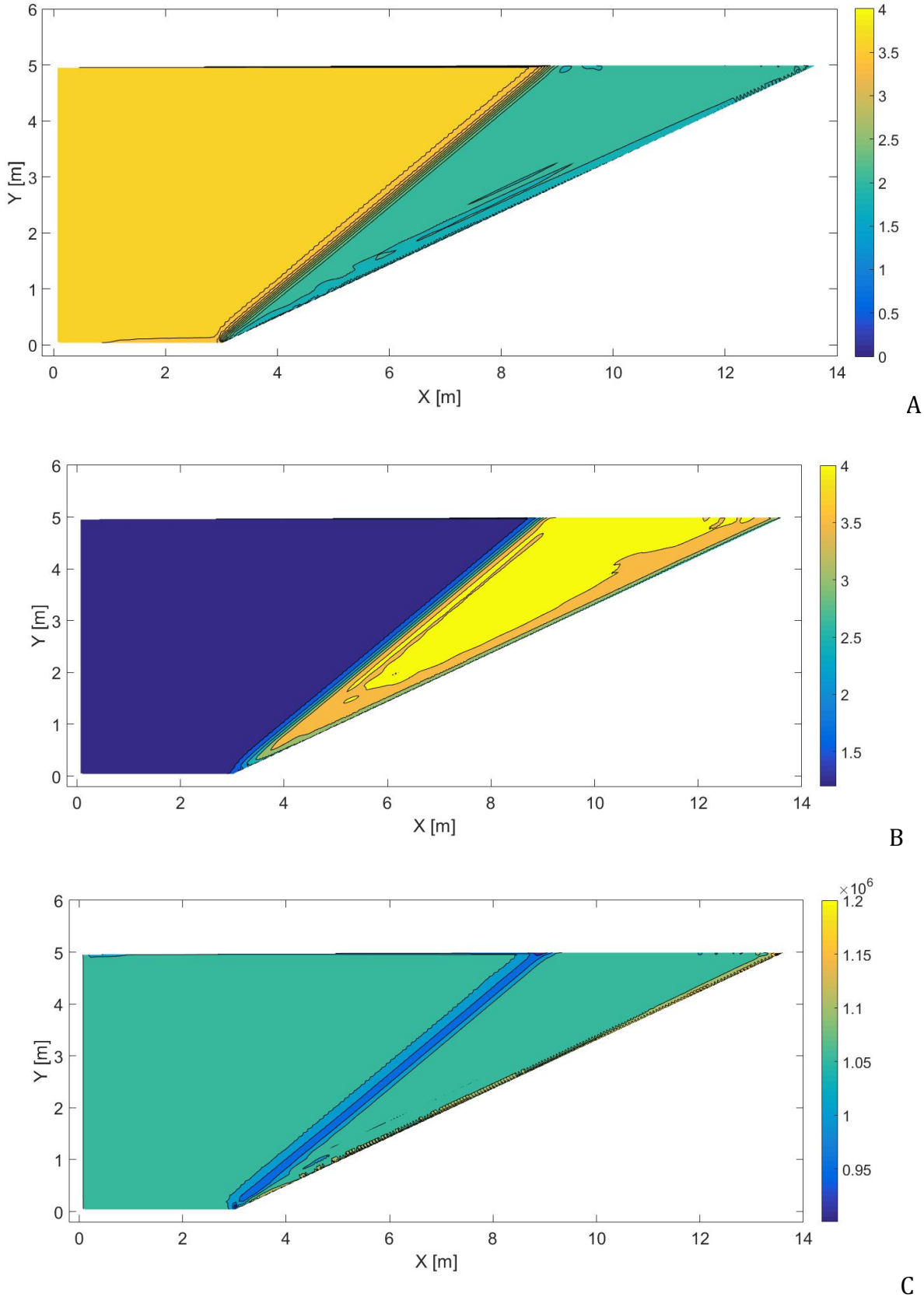

Figure 9. Contour lines of (a) Mach number, (b) density, (c) stagnation enthalpy for test case No. 3 (θ = 25°).